

CONSTRAINING THE ASSEMBLY OF NORMAL AND COMPACT PASSIVELY EVOLVING GALAXIES FROM REDSHIFT $z = 3$ TO THE PRESENT WITH CANDELS

P. CASSATA¹, M. GIAVALISCO², C. C. WILLIAMS², YICHENG GUO³, BOMEI LEE², A. RENZINI⁴, H. FERGUSON⁵, S. F. FABER³, G. BARRO³, D. H. MCINTOSH⁶, YU LU⁷, E. F. BELL⁸, D. C. KOO³, C. J. PAPOVICH⁹, R. E. RYAN⁵, C. J. CONSELICE¹⁰, N. GROGIN⁵, A. KOEKEMOER⁵, AND N. P. HATHI¹¹

¹ Aix Marseille Université, CNRS, LAM (Laboratoire d’Astrophysique de Marseille) UMR 7326, F-13388 Marseille, France; paolo.cassata@oamp.fr

² Department of Astronomy, University of Massachusetts, Amherst, MA 01003, USA

³ UCO/Lick Observatory, Department of Astronomy and Astrophysics, University of California, Santa Cruz, CA, USA

⁴ Osservatorio Astronomico di Padova (INAF-OAPD), Vicolo dell’Osservatorio 5, I-35122, Padova, Italy

⁵ Space Telescope Science Institute, 3700 San Martin Boulevard, Baltimore, MD 21218, USA

⁶ Department of Physics, University of Missouri, Kansas City, MO, USA

⁷ Kavli Institute for Particle Astrophysics and Cosmology, Stanford, CA 94309, USA

⁸ Department of Astronomy, University of Michigan, 500 Church Street, Ann Arbor, MI 48109, USA

⁹ Department of Physics and Astronomy, Texas A&M University, College Station, TX, USA

¹⁰ The School of Physics and Astronomy, University of Nottingham, Nottingham, UK

¹¹ Carnegie Observatories, Pasadena, CA 91101, USA

Received 2013 March 11; accepted 2013 July 31; published 2013 September 12

ABSTRACT

We study the evolution of the number density, as a function of the size, of passive early-type galaxies (ETGs) with a wide range of stellar masses ($10^{10} M_{\odot} < M_{*} \lesssim 10^{11.5} M_{\odot}$) from $z \sim 3$ to $z \sim 1$, exploiting the unique data set available in the GOODS-South field, including the recently obtained WFC3 images as part of the Cosmic Assembly Near-infrared Deep Extragalactic Legacy Survey. In particular, we select a sample of ~ 107 massive ($M_{*} > 10^{10} M_{\odot}$), passive (SSFR $< 10^{-2} \text{ Gyr}^{-1}$), and morphologically spheroidal galaxies at $1.2 < z < 3$, taking advantage of the panchromatic data set available for GOODS, including VLT, CFHT, *Spitzer*, *Chandra*, and *HST* ACS+WFC3 data. We find that at $1 < z < 3$ the passively evolving ETGs are the reddest and most massive objects in the universe, and we prove that a correlation between mass, morphology, color, and star formation activity is already in place at that epoch. We measure a significant evolution in the mass–size relation of passive ETGs from $z \sim 3$ to $z \sim 1$, with galaxies growing on average by a factor of two in size in a 3 Gyr timescale only. We also witness an increase in the number density of passive ETGs of 50 times over the same time interval. We find that the first ETGs to form at $z \gtrsim 2$ are all compact or ultra-compact, while normal-sized ETGs (meaning ETGs with sizes comparable to those of local counterparts of the same mass) are the most common ETGs only at $z < 1$. The increase of the average size of ETGs at $0 < z < 1$ is primarily driven by the appearance of new large ETGs rather than by the size increase of individual galaxies.

Key words: cosmology: observations – galaxies: evolution – galaxies: fundamental parameters

Online-only material: color figures

1. INTRODUCTION

Early-type galaxies (ETGs) have been the object of many studies in recent years, as they contain crucial information about the evolution of the galaxy content. First, they are by definition the oldest objects at each epoch, and they can be considered relics of the star formation activity that happened in the past; the age of the stellar populations in these galaxies at $z \sim 0$ are compatible with redshifts of formations $z > 2$ (Renzini 2006). Second, ETGs are the most massive objects in the local universe, containing the bulk of the stellar mass (Baldry et al. 2004).

Understanding the history of the assembly of these galaxies throughout cosmic time is crucial to constrain models of galaxy evolution. The first generation of extremely massive ETGs ($M_{\odot} > 10^{11}$) is already in place at $z \sim 2.5$ (Guo et al. 2012); their number density dramatically increases during the $1 < z < 3$ epoch (Ilbert et al. 2010, 2013; Cassata et al. 2011; Brammer et al. 2011), followed by a milder evolution at $0 < z < 1$ (Bell et al. 2004; Faber et al. 2007; Pozzetti et al. 2010). The overall evolution of the ETGs depends strongly on stellar mass, following a “downsizing” pattern: more massive ETGs build up preferentially earlier than the less massive ones

(Arnouts et al. 2007; Marchesini et al. 2009; Ilbert et al. 2010, 2013; Cassata et al. 2011; Brammer et al. 2011).

At the same time, the massive passive ETGs are found to have 3–5 times smaller sizes at $z > 1$ than in the local universe (Daddi et al. 2005; Trujillo et al. 2007; Toft et al. 2007; Zirm et al. 2007; Cimatti et al. 2008; Van Dokkum et al. 2008; Buitrago et al. 2008; Weinzirl et al. 2011), and thus they are 30–100 times denser. These results ignited a debate about the possible mechanism producing the size evolution: Naab et al. (2009) claim that the observed size evolution of passive ETGs can be explained by minor merger events, while Khochfar & Silk (2006) propose that the observed evolution can be explained by the variation of the amount of cold gas available during the major merger events that produce ETGs: the most massive ones formed at high- z , when major mergers were more gas-rich than at later epochs. Although López-Sanjuan et al. (2012) claimed that the observed minor mergers at $0 < z < 1$ can account for up to 55% of the size growth of ETGs, Nipoti et al. (2012) claimed that minor and major mergers with spheroids are not sufficient to explain the observed size evolution between $z \sim 2.2$ and $z \sim 1.3$.

From a theoretical point of view, some key questions on the formation and evolution of ETGs are still open. One, we still

do not know through which mechanism the ETGs assemble their mass: is it through major mergers at early epochs, as it is predicted by models of galaxy formation (Shankar et al. 2010, 2013), it is through cold accretion, a so far relatively unconstrained mechanism that is proposed to efficiently funnel large amounts of cold gas in the center of high-density regions (Dekel et al. 2009a) or is it through the collapse of unstable disks, which have been shown to be numerous at $z \sim 2$ (Genzel et al. 2008; Förster-Schreiber et al. 2009)? Two, what is the mechanism that shuts off star formation in such objects, turning them into passively evolving ETGs? The dependence of the quenched ETG population on stellar mass and environment has been recently elucidated on phenomenological grounds (Peng et al. 2010, 2012), but what remain to be understood are the concrete physical mechanisms responsible for what is referred to as *mass quenching* and *environment quenching* in these studies.

In this paper we take advantage of the wealth of data available in the Chandra Deep Field South field, mainly gathered as a part of the GOODS and Cosmic Assembly Near-infrared Deep Extragalactic Legacy Survey (CANDELS) surveys, to select a robust sample of passive ETGs at $1.2 < z < 3$, which we use to constrain the assembly of their mass content as a function of the size, complementing and completing the analysis performed in Cassata et al. (2011, C11 hereafter). In particular, we dig into the passive population down to $M_* = 10^{10} M_\odot$ up to $z \sim 3$, a mass regime between 5 and 10 times below M^* (Ilbert et al. 2010).

Throughout this paper, we use a concordance cosmological model ($\Omega_\Lambda = 0.7$, $\Omega_m = 0.3$, and $H_0 = 70 \text{ km s}^{-1} \text{ Mpc}^{-1}$), we assume a Salpeter initial mass function (IMF; lower and upper masses of 0.1 and $100 M_\odot$, respectively; Salpeter 1955), we use AB magnitudes, and we define as size of galaxies the circularized half-light radius.

2. DATA AND SAMPLE SELECTION

The GOODS-South field is the one of the best studied parts of the sky, having been imaged with all the largest available telescopes (*Hubble*, *Spitzer*, VLT, *Chandra*, *XMM*, *Herschel*, CFHT). The GOODS *HST* Treasury Program (Giavalisco et al. 2004) provides ultradeep high-resolution images in the *B*, *V*, *i*, and *z* bands. Deep ground-based imaging in the *U* band is provided by VIMOS/VLT for the CDFS (Nonino et al. 2009). Moreover, VLT/ISAAC imaged the CDFS in the *J*, *H*, and *K* bands. Ultradeep *Spitzer*/IRAC imaging is also available in the 3.6, 4.5, 5.6, and $8.0 \mu\text{m}$ MIR channels and in the $24 \mu\text{m}$ FIR one. The field has also been recently imaged with *Herschel*/PACS at 100 and $160 \mu\text{m}$ as a part of the GOODS/*Herschel* program (Elbaz et al. 2011). About 3000 spectroscopic redshifts are also available, among which 1200 are at $z > 1$ (Cimatti et al. 2008; Vanzella et al. 2008; Popesso et al. 2009; Kurk et al. 2013).

CANDELS (Grogin et al. 2011; Koekemoer et al. 2011), the largest *HST* campaign ever undertaken, is collecting high-resolution images in the F105W (*Y*-band), F125W (*J*-band) and F160W (*H*-band) filters for five of the most intensively studied extragalactic fields, namely, GOODS-South and -North, EGS, UDS, and COSMOS. In this paper we include the first four epochs of CANDELS observations in GOODS-S, that cover the central $\sim 80 \text{ arcmin}^2$ of the GOODS-S field, for a total integration time of two orbits each in F125W (*J* band) and F160W (*H* band). We include as well the WFC3 observations taken as part of the Early Release Science Program 2 (ERS2: GO 11359.

PI: O’Connell; Windhorst et al. 2011), which cover an additional $\sim 40 \text{ arcmin}^2$ area in the northern part of the GOODS-S field, with integration times of two orbits in each of the F098M (*Y*-band), F125W (*J*-band) and F160W (*H*-band) filters. The final mosaics in *Y*, *J*, and *H* bands were assembled using MultiDrizzle (see Koekemoer et al. 2011 for details), combining the data to a $0''.06$ pixel grid, and producing a point-spread function (PSF) of $\sim 0''.16$ in our resulting WFC3 images. The 1σ fluctuations of the sky for the ERS2 regions are 27.2, 26.6, and 26.3 AB arcsec^2 in the *Y*, *J*, and *H* bands, respectively; for the four-epoch CANDELS region, the 1σ fluctuations are 26.6 AB arcsec^2 for both the *J* and *H* bands.

We have built a multiwavelength catalog using the TFIT procedures by Laidler et al. (2007), using the *H* band as the detection image and including the *U* band from VIMOS, the *B*, *V*, *i*, and *z* bands from GOODS/ACS, the *Y*, *J*, and *H* bands from CANDELS/WFC3, and the *Ks* band from VLT/ISAAC (Guo et al. 2013). This procedure allows us to match the PSF of images having different resolutions and to obtain homogeneous aperture magnitudes from the different images. The catalog includes about 11,000 objects brighter than $m_H = 25.5$, 4500 of which are at $1.2 < z < 3$, according to their spectroscopic or photometric redshift (see below).

We included the spectroscopic redshifts available in literature for the GOODS-S field (Vanzella et al. 2008; Cimatti et al. 2008; Popesso et al. 2009; Kurk et al. 2013) for 2232 objects, and we measured photometric redshifts for the remaining objects, using the PEGASE 2.0 templates (Fioc & Rocca-Volmerange 1997), following the same procedure in Guo et al. (2012).

We then fitted the spectral energy distribution (SED) from UV to $8 \mu\text{m}$ to the updated version of Bruzual & Charlot (2003, CB07) in order to get accurate measurements of stellar mass, $E(B - V)$, age, and SFR of the galaxies, taking into account the uncertainty associated to the photo-*z* measures. In particular, we use a Salpeter IMF (Salpeter 1955) with lower and upper masses of 0.1 and $100 M_\odot$, we apply the Calzetti law (Calzetti et al. 2000) to describe the dust extinction, and we assume exponentially declining star formation histories $\text{SFR}(t) \propto e^{(-t/\tau)}$, where *t* is age (i.e., the time passed since the peak of the star formation) and τ is the characteristic time of the star formation event. Maraston et al. (2010) showed that these exponentially declining SFR models tend to overestimate the SFRs and underestimate stellar masses for star-forming galaxies at $z \sim 2$, while truncated exponentially increasing models give better results; however, the effect of such a different star formation history (SFH) on passively evolving galaxies has not been conducted yet, and we defer this analysis to a forthcoming paper. In any event, these SED fits are only used to identify passively evolving galaxies.

We extracted a “parent” catalog of 1051 galaxies with $M_* > 10^{10} M_\odot$ and redshift $z > 1.2$, from which we selected only passive galaxies with specific star formation rate $\text{SSFR} < 10^{-2} \text{ Gyr}^{-1}$ (332 galaxies). This SSFR limit is very restrictive: galaxies with $\text{SSFR} = 10^{-2} \text{ Gyr}^{-1}$ would need 100 Gyr to double their stellar mass, if they continue to form stars at the present rate. We then eliminated all galaxies with a late-type morphology in the *H*-band WFC3 image (based on visual inspection, similarly to C11) and we also excluded galaxies detected in the *Spitzer*/MIPS $24 \mu\text{m}$ and *Herschel*/PACS $100 \mu\text{m}$ channels. Although *Spitzer*/*Herschel* data alone do not exclusively select passive galaxies at high redshift, since their sensitivity corresponds to relatively high SFRs at high redshift, they can be useful to remove dusty objects for

which the SED fitting process might lead to wrong determinations of mass and SFH. We find that the *Spitzer*/*MIPS* condition is more restrictive than the *Herschel*/*PACS* one, with more objects detected in *MIPS* than in *Herschel*, and with all objects detected in *Herschel* also detected in *MIPS*. In the end, we removed 18 objects due to these restrictions, ensuring that the SFR is lower than 5 and $20 M_{\odot} \text{ yr}^{-1}$ at $z \sim 1.2$ and $z \sim 2$, respectively (Elbaz et al. 2011). The resulting sample of passive ETGs contains 107 galaxies, 28 of which have a spectroscopic redshift. For the remainder of this paper, we define “ETGs” as galaxies that are passive according to our criteria (SSFR and no detection in *Herschel*/*Spitzer*) and have a spheroidal morphology. Of the resulting 107 passive morphologically spheroidal ETGs, 84% and 92% have Sérsic indices $n > 2$ and $n > 2.5$, respectively (similarly to Bell et al. 2012). This ensures that our sample is not contaminated by quiescent disks as in van der Wel et al. (2011).

We used the GALFIT package (Peng et al. 2002) to fit the light profile in the *H* band (matching the rest-frame optical up to $z \sim 3$):

$$I(r) = I_e \exp \left\{ -b_n \left[\left(\frac{r}{r_e} \right)^{1/n} - 1 \right] \right\}, \quad (1)$$

where $I(r)$ is the surface brightness measured at distance r , I_e is the surface brightness at the effective radius r_e , and b_n is a parameter related to the Sérsic index n . For $n = 1$ and $n = 4$ the Sérsic profile reduces, respectively, to an exponential and a de Vaucouleurs profile. Bulge dominated objects typically have high n values (e.g., $n > 2$) and disk dominated objects have n around unity. The PSF was obtained in each passband needed by averaging well-exposed, unsaturated stars. We run GALFIT, experimenting on various sizes of the fitting region around each galaxy, and with the sky either set to a pre-measured value or left as a free parameter. We verified that the sizes and Sérsic indices do not vary by more than 10% in the various cases. The values that we show throughout the paper were obtained with a free sky and $6 \times 6 \text{ arcsec}^2$ fitting regions. Any close-by object detected by SExtractor within each fitting region was automatically masked out during the fitting procedure.

We report in Table 1 the relevant properties of the 107 ETGs in our sample. For each galaxy, we indicate coordinates, redshift, stellar mass, SSFR, Sérsic index, and circularized half-light radius.

Since one of the aims of this study is to follow the evolution of the mass–size relation for ETGs as a function of the redshift, from low- ($z \sim 0.2$) to high-redshift ($z \sim 2.5$), we have to thoroughly determine the mass completeness and the robustness of the size measurements for our sample, across the whole explored redshift range. The final mass completeness of the sample will depend on (1) the detection probability (linked to the *H*-band magnitude, since the catalog is *H*-band-detected) and (2) our ability to measure robust photometric redshifts for objects that are included in the photometric catalog.

The completeness of the *H*-band catalog that we use in this work has been tested with Monte Carlo simulations, which showed that down to magnitude 25.5, for typical $z \sim 2$ spheroids with $R_e = 0''.125$, the catalog is 80% complete (Grogan et al. 2011; Guo et al. 2013). Briefly, artificial galaxies with a mix of luminosity, SED (from star-forming to passive) and morphology (disk and de Vaucouleurs spheroids) with size extracted from a log-normal distribution have been added to the CANDELS images and then detected and analyzed using the

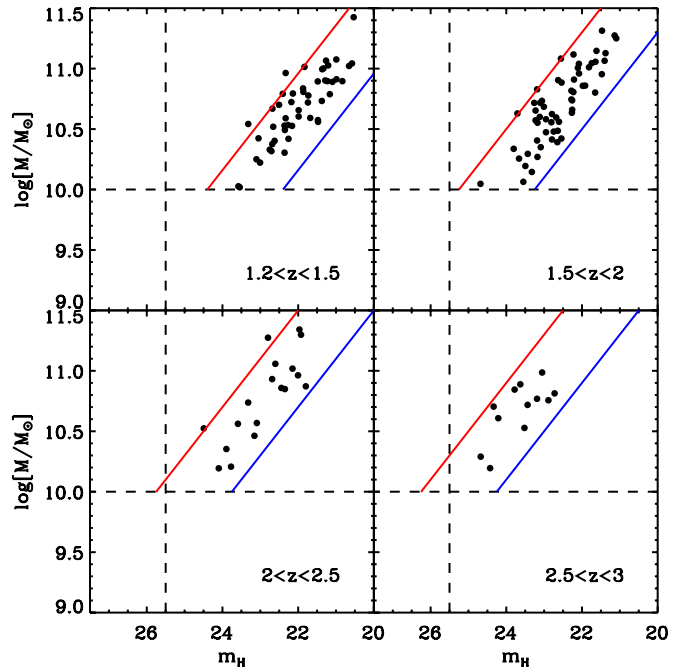


Figure 1. Stellar mass vs. AB magnitude in the WFC3/F160W *H*-band filter in four redshift bins: $1.2 < z < 1.5$, $1.5 < z < 2$, $2 < z < 2.5$, and $2.5 < z < 3$. The vertical dashed line at $m_{F160W} = 25.5$ indicates the magnitude at which the CANDELS *H*-band images are 80% complete, the dashed horizontal line at $M/M_{\odot} = 10^{10}$ shows the mass limit of our sample, and the red and blue diagonal lines indicate, for each redshift bin, the stellar mass vs. *H*-band magnitude relation for the reddest and bluest models available in our template grid.

(A color version of this figure is available in the online journal.)

same procedures adopted for the real ones. Completeness was then measured from the rate of successful identifications.

The *H*-band magnitude at which the photometric catalog is 80% complete of course translates to different stellar masses at different redshifts for galaxies with different ages and M/L ratios. Figure 1 shows precisely how the *H*-band magnitude depends on the stellar mass, as a function of the redshift, for passive galaxies with different M/L ratios (the reddest and bluest models are shown in red and blue, respectively). As expected, the real galaxies generally lie to the right of the reddest model, meaning that, for a given stellar mass, they are brighter than the model. So, from Figure 1, we learn that up to $z \sim 3$ even the reddest galaxies with $M > 10^{10} M_{\odot}$ (the ones with faintest *H*-band magnitudes) are brighter than $m_H = 25.5$, which is also the 80% completeness limit of the CANDELS *H*-band images from which the catalog is extracted. So, this analysis robustly assesses the probability that a galaxy with $M > 10^{10} M_{\odot}$, with colors compatible with being passive and with redshift $1.2 < z < 3$, is detected in the *H*-band images and thus included in our photometric catalog.

Moreover, most of our ETGs have *H*-band magnitudes brighter than $m_H = 24$, which is very bright in terms of the sensitivity reached by the CANDELS observations. The GOODS optical observations in the CDFS area are as deep as 27.5–28 mag in the *B*, *V*, *i*, and *z* bands, allowing us to easily sample the Balmer break of the ETGs in our sample at $z > 1.2$. In fact, 95% of the 107 ETGs in our sample at $1.2 < z < 3$ are detected in the *i* and/or *z* bands. At this flux levels photometric redshifts are very accurate, especially for SEDs, such as that of ETGs, where strong spectral gradients are present. The accuracy of photometric redshift and SED fitting has been the subject of extensive testing using both spectroscopy and Monte Carlo

Table 1
The Sample of $1.2 < z < 3$ ETGs

ID	R.A.	decl.	Redshift	$\log(M_*)$	$\log(\text{SSFR})$ (Gyr^{-1})	n	R_e (kpc)
1	53.0630013	-27.8831943	1.726	10.88	-3.40	4.27 ± 0.17	0.48 ± 0.10
2	53.0631728	-27.8823861	1.945	10.05	-2.16	4.03 ± 1.02	0.82 ± 0.16
3	53.0586055	-27.880579	1.514	10.39	-2.99	3.31 ± 0.15	0.62 ± 0.12
4	53.0656657	-27.878867	2.064	10.96	-2.99	5.87 ± 0.13	0.96 ± 0.19
5	53.0665509	-27.8744763	2.071	10.19	-2.16	5.39 ± 0.84	0.64 ± 0.13
6	53.1192783	-27.8737417	1.815	10.66	-2.12	2.51 ± 0.17	1.10 ± 0.22
7	53.1161476	-27.8719157	1.843	11.08	-11.65	3.17 ± 0.09	1.09 ± 0.22
8	53.158032	-27.8685091	1.647	10.41	-2.99	2.34 ± 1.82	1.87 ± 0.45
9	53.103651	-27.8610611	1.572	10.56	-3.40	3.61 ± 0.11	0.66 ± 0.13
10	53.1305966	-27.8590248	1.336	10.72	-2.12	6.11 ± 0.13	2.02 ± 0.40
11	53.1315313	-27.8582558	1.279	10.03	-7.32	2.30 ± 0.13	0.65 ± 0.13
12	53.1075669	-27.8556805	2.559	10.70	-2.12	4.07 ± 0.41	1.85 ± 0.37
13	53.202157	-27.8508707	1.550	10.34	-2.16	1.34 ± 0.12	0.94 ± 0.19
14	53.0623203	-27.8512569	1.679	10.56	-2.12	1.74 ± 0.03	2.06 ± 0.41
15	53.2190866	-27.8451944	1.575	10.35	-2.99	2.55 ± 0.09	2.32 ± 0.46
16	53.0291339	-27.8394081	1.320	10.53	-2.99	4.61 ± 0.14	1.44 ± 0.29
17	53.026011	-27.837371	2.470	10.56	-2.99	1.82 ± 0.22	0.55 ± 0.11
18	53.1092202	-27.835699	1.493	10.42	-2.12	6.01 ± 0.23	3.64 ± 0.73
19	53.1019564	-27.834561	2.779	10.89	-2.99	3.23 ± 0.17	0.67 ± 0.13
20	53.1271313	-27.8345618	1.560	11.06	-2.99	2.73 ± 0.02	1.85 ± 0.37
21	53.1501905	-27.8345295	1.612*	10.95	-2.99	4.14 ± 0.03	1.97 ± 0.39
22	53.0341341	-27.8334496	1.307	10.38	-2.99	2.50 ± 0.10	0.80 ± 0.16
23	53.1562991	-27.8332899	1.472	10.54	-5.56	6.94 ± 0.61	0.21 ± 0.04
24	53.209139	-27.83363	1.297*	10.30	-2.12	2.41 ± 0.05	0.39 ± 0.08
25	53.0468149	-27.8330582	1.242	10.84	-2.12	5.30 ± 0.09	1.01 ± 0.20
26	53.192115	-27.8315211	1.204	10.49	-3.40	5.06 ± 0.12	0.53 ± 0.11
27	53.1234414	-27.8282105	2.596	10.23	-2.12	4.41 ± 0.73	0.58 ± 0.12
28	53.1295626	-27.8276486	1.519	10.58	-2.16	4.15 ± 0.14	0.63 ± 0.13
29	53.1716978	-27.8256614	1.672	10.86	-2.12	4.15 ± 0.05	1.21 ± 0.24
30	53.1514426	-27.8258671	1.465	10.79	-2.16	3.97 ± 0.06	1.03 ± 0.21
31	53.1862211	-27.8252019	1.980	10.48	-2.98	4.16 ± 0.11	0.33 ± 0.07
32	53.1861355	-27.8233989	1.363	10.53	-2.99	4.25 ± 0.08	1.16 ± 0.23
33	53.0355921	-27.8197025	1.346	11.03	-3.40	5.00 ± 0.05	1.20 ± 0.24
34	53.2166762	-27.8143395	1.570	10.68	-2.16	1.23 ± 0.03	0.83 ± 0.17
35	53.1632194	-27.8089859	2.670*	10.72	-2.12	0.97 ± 0.06	0.48 ± 0.10
36	53.0999352	-27.8084462	2.045	10.46	-2.12	3.62 ± 0.16	0.36 ± 0.07
37	53.1165086	-27.8067451	2.317	10.85	-2.12	3.89 ± 0.08	0.61 ± 0.12
38	53.0447273	-27.8053844	1.676	10.96	-7.32	2.87 ± 0.04	0.75 ± 0.15
39	53.123105	-27.8033913	2.326	11.02	-2.12	5.66 ± 0.13	0.52 ± 0.10
40	53.2298705	-27.7984197	1.696	10.25	-2.99	5.94 ± 0.84	0.61 ± 0.12
41	53.1629996	-27.7976541	1.541*	10.55	-2.12	2.71 ± 0.12	0.35 ± 0.07
42	53.1403096	-27.7975248	1.687	10.49	-2.99	4.00 ± 0.00	1.36 ± 0.27
43	53.1588073	-27.7971544	1.921*	10.81	-2.99	5.07 ± 0.13	0.38 ± 0.08
44	53.2143151	-27.7963366	1.299*	10.33	-2.16	4.32 ± 0.12	3.00 ± 0.60
45	53.1242367	-27.7953627	2.659	10.19	-2.12	2.68 ± 0.31	0.37 ± 0.07
46	53.0223014	-27.7927552	2.521	10.77	-2.12	5.68 ± 0.90	0.36 ± 0.07
47	53.2306473	-27.7925608	1.213	10.89	-2.99	6.79 ± 0.10	2.42 ± 0.48
48	53.2023127	-27.7854291	1.422	10.70	-7.31	5.55 ± 0.15	0.67 ± 0.13
49	53.1357319	-27.7849289	1.301	10.25	-7.32	4.33 ± 0.15	0.57 ± 0.11
50	53.165163	-27.7858695	1.317*	10.90	-2.12	4.84 ± 0.04	4.46 ± 0.89
51	53.0924271	-27.7832531	1.758	10.62	-2.99	5.16 ± 0.18	0.50 ± 0.10
52	53.0349172	-27.7808879	1.277*	10.56	-2.99	5.16 ± 0.79	2.36 ± 0.47
53	53.1027215	-27.7776062	1.660	10.47	-2.12	4.24 ± 0.17	0.43 ± 0.09
54	53.0469492	-27.7751149	1.487	10.02	-2.99	3.01 ± 0.13	1.26 ± 0.25
55	53.0522039	-27.7747713	1.605*	11.19	-2.99	2.09 ± 0.01	2.06 ± 0.41
56	53.0457468	-27.7731917	1.555	10.41	-3.40	6.20 ± 0.33	1.55 ± 0.31
57	53.0466115	-27.7721866	1.604	10.60	-2.16	3.38 ± 0.09	1.09 ± 0.22
58	53.0758023	-27.7711325	1.669	10.65	-2.12	2.57 ± 0.10	0.67 ± 0.13
59	53.1033384	-27.7716345	1.306*	11.00	-3.40	7.06 ± 0.08	1.85 ± 0.37
60	53.0700699	-27.7680563	1.874	10.73	-7.32	3.27 ± 0.11	0.57 ± 0.11
61	53.1191583	-27.7657612	1.756	10.72	-7.31	3.84 ± 0.19	0.45 ± 0.09
62	53.1410199	-27.7667256	1.903*	11.31	-2.12	6.57 ± 0.07	2.26 ± 0.45
63	53.0219254	-27.7645642	1.379	10.72	-2.99	7.35 ± 0.24	2.42 ± 0.48
64	53.1094393	-27.7640869	1.222*	10.73	-2.99	7.14 ± 0.07	3.00 ± 0.60
65	53.1397065	-27.7631971	2.086	10.74	-2.16	4.33 ± 0.18	1.91 ± 0.38

Table 1
(Continued)

ID	R.A.	decl.	Redshift	$\log(M_*)$	$\log(\text{SSFR})$ (Gyr^{-1})	n	R_e (kpc)
66	53.222464	-27.7612737	1.492	10.59	-2.99	5.58 ± 0.29	0.56 ± 0.11
67	53.0436907	-27.7608963	1.536	10.06	-2.99	2.99 ± 0.29	0.74 ± 0.15
68	53.0885413	-27.7600014	1.711	10.19	-2.12	5.97 ± 0.41	1.08 ± 0.22
69	53.1095536	-27.7600489	1.222*	10.79	-2.12	1.83 ± 0.01	0.55 ± 0.11
70	53.0467174	-27.7592896	1.215*	10.91	-2.99	2.16 ± 0.02	0.98 ± 0.20
71	53.0283891	-27.7567659	1.374*	10.59	-2.12	4.24 ± 0.11	0.86 ± 0.17
72	53.1098346	-27.7539157	1.309*	10.53	-2.12	2.97 ± 0.09	3.38 ± 0.68
73	53.1745726	-27.7533753	1.848*	10.91	-2.12	2.05 ± 0.03	0.97 ± 0.19
74	53.0262756	-27.7507663	1.291	10.40	-3.40	2.79 ± 0.08	0.60 ± 0.12
75	53.0126525	-27.7472438	2.573*	10.81	-2.12	1.93 ± 0.07	0.52 ± 0.10
76	53.1210056	-27.7422814	1.202*	10.79	-11.65	2.06 ± 0.04	0.79 ± 0.16
77	53.1200496	-27.7418008	1.944	10.72	-2.98	4.63 ± 0.24	1.71 ± 0.34
78	53.1587781	-27.7423834	1.221*	11.04	-2.16	7.38 ± 0.07	7.86 ± 1.57
79	53.0371183	-27.7402076	2.733	10.61	-2.12	6.21 ± 0.95	0.54 ± 0.11
80	53.0468655	-27.7386696	1.563	10.57	-3.60	4.29 ± 0.18	0.63 ± 0.13
81	53.0309142	-27.7381823	1.514	10.64	-2.99	4.51 ± 0.10	0.82 ± 0.16
82	53.011809	-27.7360329	2.605	10.29	-2.12	5.39 ± 0.99	0.80 ± 0.16
83	53.0034075	-27.7317028	1.261	11.43	-5.56	4.89 ± 0.04	2.99 ± 0.60
84	53.0642415	-27.7276216	1.551	11.04	-7.31	7.43 ± 0.19	2.74 ± 0.55
85	53.0168731	-27.7258547	2.534	10.84	-3.40	3.22 ± 0.25	0.49 ± 0.10
86	53.0596296	-27.7257921	1.609*	10.66	-2.99	2.66 ± 0.06	0.73 ± 0.15
87	53.062823	-27.7264618	1.514	11.25	-2.16	3.38 ± 0.02	1.68 ± 0.34
88	53.1080155	-27.7253183	1.530	10.26	-2.12	1.37 ± 0.06	1.38 ± 0.28
89	53.0584748	-27.7230903	2.224	10.48	-7.32	5.23 ± 0.67	0.72 ± 0.14
90	53.124966	-27.7229558	1.604*	10.82	-3.40	1.95 ± 0.03	1.04 ± 0.21
91	53.0246009	-27.722114	2.403	10.52	-7.32	2.91 ± 1.01	0.16 ± 0.03
92	53.1304855	-27.7211527	1.415*	11.01	-2.12	2.92 ± 0.03	2.12 ± 0.42
93	53.1873642	-27.719186	2.324	10.87	-2.12	3.28 ± 0.08	0.42 ± 0.08
94	53.1283436	-27.7184149	1.652	10.74	-2.12	3.77 ± 0.07	1.56 ± 0.31
95	53.1279381	-27.7188853	1.634	11.15	-3.40	4.25 ± 0.05	2.81 ± 0.56
96	53.1853485	-27.7173246	2.346	10.35	-2.12	5.29 ± 0.42	0.67 ± 0.13
97	53.0961051	-27.7163092	1.527	10.27	-2.12	6.76 ± 0.39	2.17 ± 0.43
98	53.1527343	-27.7162517	1.614*	11.04	-3.40	3.95 ± 0.04	1.13 ± 0.23
99	53.1164048	-27.7127033	1.610*	10.86	-2.99	3.76 ± 0.05	0.64 ± 0.13
100	53.1274224	-27.712065	1.698	11.12	-11.65	6.57 ± 0.17	1.16 ± 0.23
101	53.1496036	-27.711374	1.612*	11.01	-2.99	5.91 ± 0.12	1.64 ± 0.33
102	53.17976	-27.7116773	1.416*	11.07	-3.40	6.46 ± 0.07	2.52 ± 0.50
103	53.1085226	-27.7101495	1.609*	11.24	-5.56	4.21 ± 0.05	0.81 ± 0.16
104	53.0776676	-27.6956726	1.370	10.22	-2.99	3.15 ± 0.12	0.60 ± 0.12
105	53.061039	-27.6934857	1.363	11.00	-2.16	5.27 ± 0.07	1.66 ± 0.33
106	53.0969607	-27.6793971	1.795	10.60	-2.99	3.15 ± 0.19	0.84 ± 0.17
107	53.1167317	-27.6753427	1.568	10.42	-2.99	5.04 ± 0.25	0.32 ± 0.06

Note. For each ETG in our sample, we report the celestial coordinates, the redshift (stars mark spectroscopic), stellar masses M_* , SSFR, Sérsic indices n , and circularized effective radii R_e .

simulations. For our galaxies in our redshift range we find small scatter ($\sigma \sim 0.05$) and low number of outliers (2%; Dahlen et al. 2013). When CB07 models are fit to the SEDs to get physical parameters such as mass and SFR, the uncertainty in the photo- z measures is taken into account. This analysis allows us to conclude that our sample is complete down to $M = 10^{10} M_\odot$ up to $z \sim 3$.

The second key point in our analysis is our ability to robustly measure the size of galaxies at $1.2 < z < 3$. Ravindranath et al. (2006), Cimatti et al. (2008), Trujillo et al. (2007), and van der Wel et al. (2012) showed that GALFIT yields unbiased estimates of the Sérsic index and effective radius for galaxies with $S/N > 10$ and $r_e > 0''.03$, independently of the redshift of the source. In fact, despite galaxies having 40 times fainter surface brightnesses at $z \sim 2$ than at $z \sim 0.2$, GALFIT has been proven to be able to distinguish normal and compact ETGs at $z \sim 2$. For

example, simulations in van der Wel et al. (2012) contain both compact and normal-sized ETGs at $z \sim 2$. Galaxies with stellar masses $10^{10} < M_\odot < 10^{11.5}$ have at $z \sim 2$ H -band magnitudes $22 < \text{mag}_H < 26$ (see Figure 1) and half-light radii ranging from 0.5 to 10 kpc (Figure 3). These physical sizes correspond to $0''.05$ and $1''.25$ at $z \sim 2$, respectively ($1''$ corresponds to about 8 kpc at $z \sim 2$). The simulations in van der Wel et al. (2012) fully cover these magnitude and size ranges, for galaxies with a variety of Sérsic indices and axial ratios. These same simulations show that for galaxies brighter than $m_H = 24.5$ the systematic errors are virtually absent and the random errors are around 20%, demonstrating that the measurements for the galaxies in our sample, virtually all of which brighter than $m_H = 24.5$, are robust. Moreover, the same simulations demonstrate as well that we are not missing a population of faint and large ETGs. In fact, galaxies with stellar mass around $10^{10} M_\odot$ are still brighter

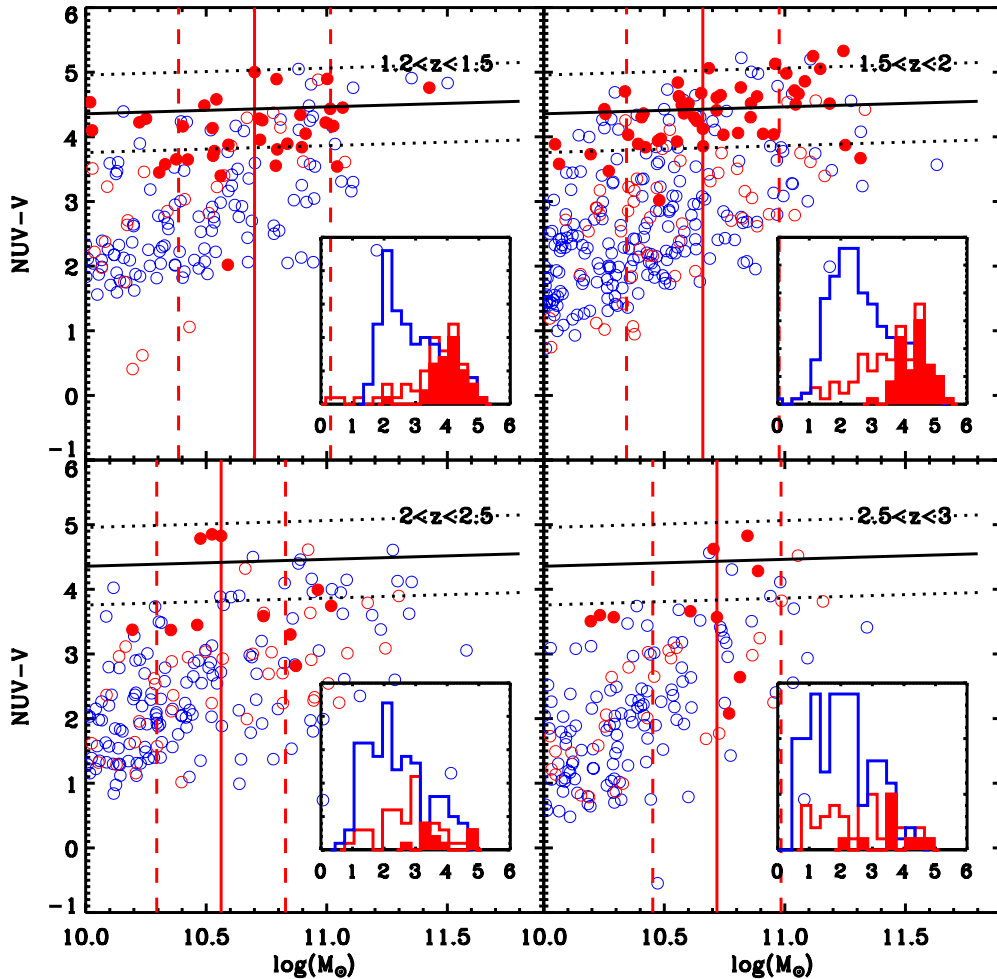


Figure 2. $N_{UV}-V$ color vs. mass in the optical rest frame for in four redshift bins: $1.2 < z < 1.5$, $1.5 < z < 2$, $2 < z < 2.5$, and $2.5 < z < 3$. The filled circles, red empty circles, and blue empty circles represent the passive early-type galaxies (spheroidal morphology and $SSFR < 10^{-2}$), the morphologically early-type galaxies, and the morphologically late-type galaxies, respectively. The black continuous and dashed lines show a fit to the ETGs in the first two bins combined. The insets show the color distribution in each bin, with the same color coding as the large figures. The red continuous and dotted lines show the median mass and scatter for the ETGs in the four redshift bins.

(A color version of this figure is available in the online journal.)

than magnitude 25.5 at $z \sim 2.5$ (see Figure 1): van der Wel’s simulations show that even for those faint galaxies, systematic errors are within control and random errors are around 50% at the most (large, but still reasonable). We note that as soon as we move to $M_{\odot} = 10^{10.5}$ at $z \sim 2.5$ the situation improves significantly, as those galaxies are even brighter than $m_H = 24.5$ and thus the random errors significantly decrease.

3. THE COLOR–MASS DIAGRAM AT $1.2 < z < 3$

In Figure 2 we show the N_{UV} color–mass diagram in four redshift bins ($1.2 < z < 1.5$, $1.5 < z < 2$, $2 < z < 2.5$ and $2.5 < z < 3$) for the “parent” catalog (empty circles) and the ETGs (filled red circles). The absolute magnitudes for the N_{UV} and V filters are computed by interpolating the observed photometry at the location expected for the *Galaxy Evolution Explorer* N_{UV} 2500 Å and Johnson V 5500 Å, respectively. We separate the parent catalog in morphologically early- and late-types, based on the visual H -band morphology.

We observe a color bimodality up to $z \sim 2$, similarly to Cassata et al. (2008), with the red peak dominated by ETGs and the blue distribution dominated by star-forming late-type galaxies. At $z > 2$ the color distribution is unimodal, but still the red galaxies are on average more massive than the blue ones.

In the two highest redshift bins, the bulk of objects displays blue colors and only a “tail” of red objects is present. Only about 50% of the galaxies on the red sequence at such redshift are passive according to our criteria.

We note that the ETGs are the reddest and most massive objects, and that the red sequence is mostly populated by galaxies with $M_* > 10^{10.5} M_{\odot}$, at all redshifts. The average mass for ETGs in the four redshift bins is around $M_* = 10^{10.7} M_{\odot}$, with a dispersion of 0.2 dex. This shows that the most massive ETGs are the first to form at $z > 1.2$, and that, as cosmic time goes by, new low-mass ETGs are formed. This result confirms earlier findings that the most massive galaxies are the first to be quenched (e.g., Bundy et al. 2006; Franceschini et al. 2006; Cimatti et al. 2006) and is in qualitative agreement with the phenomenological model of Peng et al. (2010).

We see that there is a clear correlation between the morphology, the color, and the star formation activity of the galaxies, at least up to $z = 2$: morphological ETGs are typically red and passive; morphological late-types are blue and star forming. This is in good agreement with Whitaker et al. (2011), who found a red sequence up to $z \sim 3.5$ (but the authors did not analyze the morphology of the galaxies on the red sequence), and Bell et al. (2012). These findings imply that the Hubble sequence, in

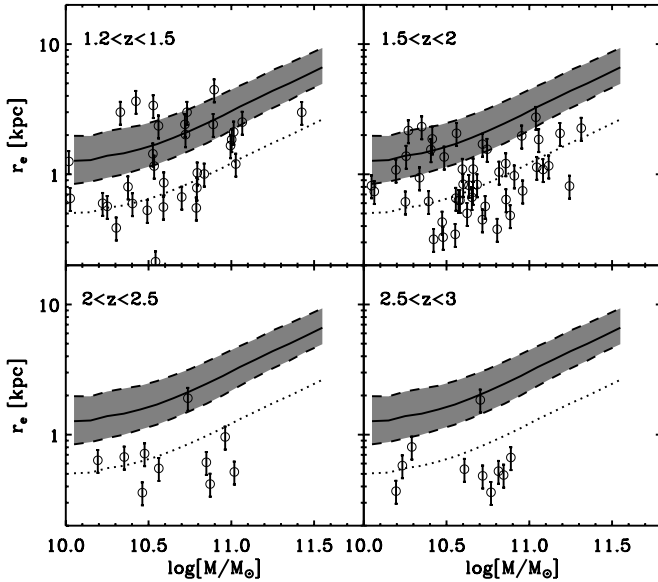


Figure 3. Mass–size relation in the optical rest frame for in four redshift bins: $1.2 < z < 1.5$, $1.5 < z < 2$, $2 < z < 2.5$, and $2.5 < z < 3$. The minimum error bars on half-light radii are set to $\pm 20\%$, if the error provided by GALFIT is smaller. This is the typical systematic error estimated via simulations for objects of comparable magnitude (van der Wel et al. 2012). The error associated with the mass estimates, as derived from the SED fitting procedure, are on the order of $\pm 10\%$, far smaller than the uncertainties due to the choice of the IMF and the set of stellar population models (Salimbeni et al. 2009). Thus, we report in the bottom right part of each panel a representative error bar on the stellar mass of ± 0.2 dex. In all bins, the gray filled region indicates the locus occupied by SDSS passive galaxies at $0 < z < 0.1$: the continuous line shows the median of the distribution, and the dashed lines contain 68% of the objects (from C11). The dotted line indicates the locus of galaxies 0.4 dex smaller than local SDSS counterparts of the same mass. Galaxies below this line are defined as ultra-compact according to C11.

the sense of a correlation between stellar mass, star formation properties, and morphology as observed in the local universe, is already in place at $z \sim 3$. The mere existence of ETGs at $z \sim 3$ indicates that such objects formed and were quenched at even higher redshift; our estimate of the age is not accurate

enough to accurately age-date the bulk of the stellar component of such objects, but presumably they accreted the bulk of their mass about 1 Gyr prior to the observation, implying a formation redshift $z \sim 5$ (similar to Gobat et al. 2012).

4. THE MASS–SIZE RELATION FOR EARLY-TYPE GALAXIES AT $1 < z < 3$

In Figure 3 we show the mass–size relation for the 107 massive ETGs at $1.2 < z < 3$ in four redshift bins. The size is measured in the WFC3 *H* band and matches the optical rest frame in the whole redshift range. The plot also shows the mass–size relation for local ETGs drawn from the Sloan Digital Sky Survey (SDSS) as derived by C11, according to whom galaxies below the SDSS local relation (the gray strip in Figure 3) are defined as compact ETGs (by definition, 17% of local ETGs are compact), and those more than 0.4 dex smaller than local counterparts of the same mass (the dotted line in Figure 3) are defined as ultra-compact. According to these definitions, compact and ultra-compact galaxies with a stellar mass $M_* = 10^{10.5} M_\odot$ have respective sizes smaller than about 1 and 0.5 kpc. In our sample, at $2.5 < z < 3$, $2 < z < 2.5$, $1.5 < z < 2$, and $1.2 < z < 1.5$, respectively $\sim 90\%$ ($\sim 70\%$), $\sim 90\%$ ($\sim 60\%$), $\sim 80\%$ ($\sim 50\%$), and $\sim 70\%$ ($\sim 40\%$) of the ETGs are compact (ultra-compact) ETGs. We performed a series of two-dimensional Kolmogorov–Smirnov tests, with the aim of checking if the mass–size distributions shown in Figure 3 statistically differ from the local ones, and if they differ in comparison with each other. We find that the probability that each of the four high- z mass–size distributions and the local SDSS galaxies are drawn from the same distribution is lower than 10^{-5} . So, in other words, the high- z distributions and the local one do differ, implying a strong evolution of the size at fixed stellar mass. However, the small size of the high- z samples prevents us from reliably quantifying the evolution from $z \sim 3$ to $z \sim 1$. We will use the full five-field CANDELS data to further investigate this issue.

In Figure 4 we report the size as a function of the redshift for our sample of 107 massive ETGs at $1.2 < z < 3$, together

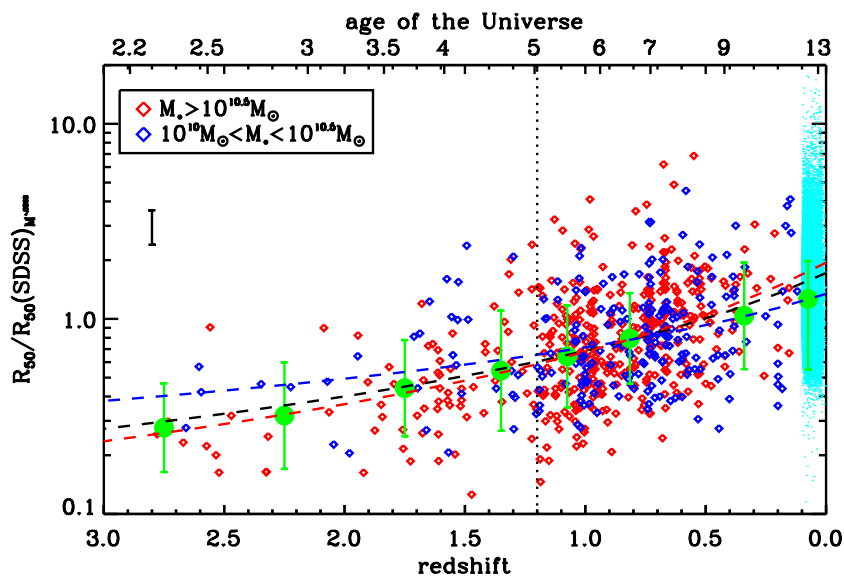


Figure 4. Evolution of the size for passive ETGs with $M_* > 10^{10} M_\odot$ and $\text{SSFR} < 10^{-2} \text{ Gyr}^{-1}$ at $0 < z < 3$, normalized to the SDSS. The blue and red points represent ETGs with $M_* < 10^{10.5} M_\odot$ and with $M_* > 10^{10.5} M_\odot$, respectively. Measures at $z < 1.2$ (indicated by the dotted vertical line) come from C11. The green filled circles with their error bars represent the median size and scatter in bin of redshift. The black, blue, and red dashed lines show the best fit for all the ETGs, the ETGs with $M_* < 10^{10.5} M_\odot$, and ETGs with $M_* > 10^{10.5} M_\odot$, respectively. The error bar at (2.8, 3) shows the typical error bar associated to the size measurement.

(A color version of this figure is available in the online journal.)

with data at $0 < z < 1.2$ from C11: measurements for ETGs at $0.3 < z < 1.2$ are done in the z band, which matches the optical rest frame (see C11 for details); ETGs in the local universe ($0 < z < 0.1$) are drawn from the SDSS, and the measurements of their sizes are taken by the DR7 NYU Value-Added Galaxy Catalog (Blanton et al. 2005; see C11 for details). Galaxy sizes are normalized to the average size of the SDSS ETGs with the same stellar mass. We also tried to normalize the size to the best-fit $R_e \propto M_{\odot}^{0.55}$ relation for each redshift (as for example in Cimatti et al. 2012), but the essence of the results discussed here did not change. In the same figure, we report the median normalized size for eight redshifts, along with the scatter of the distribution: the 1σ standard deviation of the distribution is about 0.25 dex at all redshifts. We parameterize the evolution of the average size as $\langle r_e \rangle \propto (1+z)^{\alpha}$, and we fitted the global population of ETGs, as well as ETGs with $M \leq M^{10.5} M_{\odot}$ separately. To avoid the fit being completely driven by the $\sim 100,000$ SDSS galaxies at $0 < z < 0.1$, we exclude them from the fit. We find $\alpha = -1.29 \pm 0.10$ for the global population of ETGs, $\alpha = -0.89 \pm 0.16$ for ETGs with $M_* < M^{10.5} M_{\odot}$ and $\alpha = -1.50 \pm 0.12$ for ETGs with $M_* > M^{10.5} M_{\odot}$. This means that the size evolution is faster for high-mass ETGs than for the low-mass ones, in qualitative agreement with Ryan et al. (2012). Interestingly, this result does not change if only the C11 galaxies with $z < 1.2$ are included in the fit: we find $\alpha = -1.18 \pm 0.15$, $\alpha = -0.90 \pm 0.22$, and $\alpha = -1.33 \pm 0.18$ for all the ETGs, the ETGs with $M_* < M^{10.5} M_{\odot}$ and the ETGs with $M_* > M^{10.5} M_{\odot}$, respectively.

These values are in good agreement with results by Cimatti et al. (2012), who found $-1.25 < \alpha < -0.8$, and are slightly lower (in absolute value) than the value published by Damjanov et al. (2011), who found $\alpha = -1.62$. However, we stress that the sample used here (the 107 ETGs at $z > 1.2$ plus the ETGs at $z < 1.2$ by C11) is complete in mass down to $M_* = 10^{10} M_{\odot}$ up to $z = 3$, and it was selected according to the same criteria at all redshifts, and thus is more homogeneous and complete than the ones used in these works, which are compilations of different samples published in the literature.

5. EVOLUTION OF THE NUMBER DENSITY IN PASSIVE GALAXIES AT $1 < z < 3$

In Section 4 we saw that the mass–size relation of massive ETGs evolves fast with the redshift between $z \sim 3$ and $z \sim 1.2$: at $z > 2$ about 90% of the ETGs are compact (i.e., 1σ below the local relation), with that fraction dropping to 70% at $z \sim 1.2$. From Figure 4 we also learned that the average size of ETGs roughly doubles over the same redshift interval. The evolution of the average size of galaxies illustrated in Figure 4 can be driven by two simultaneous processes: the size increase of each galaxy, possibly due to (minor) dry mergers (e.g., Naab et al. 2007; Nipoti et al. 2012; Oser et al. 2012) and to the appearance of new ETGs with a size distribution progressively shifted to larger sizes (Valentinuzzi et al. 2010a, 2010b; Cassata et al. 2011; Newman et al. 2012; Poggianti et al. 2012; Carollo et al. 2013). We know that the number density of ETGs dramatically increases with cosmic time (i.e., Ilbert et al. 2010; Pozzetti et al. 2010), hence the size evolution cannot be entirely attributed to the former mechanism, as it has been recently attempted by Oser et al. (2012). In order to try to constrain the relative importance of the two mechanisms, in this section we study the number density of ETGs of different physical sizes as a function of the redshift and the cosmic time.

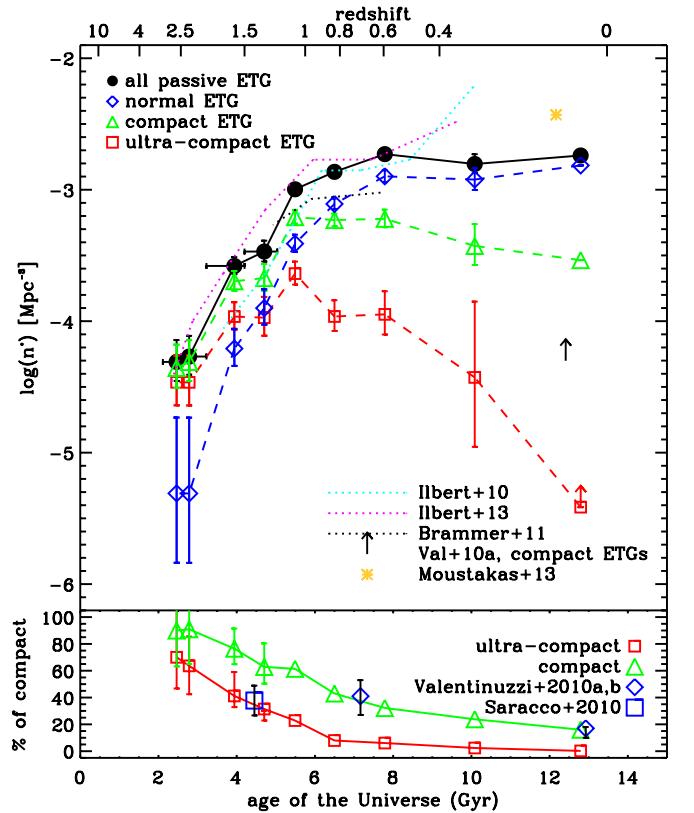


Figure 5. Top panel: number density as a function of the age of the universe and redshift of all ETGs (black circles), normal size ETGs (blue diamonds), compact ETGs (green triangles), and ultra-compact ETGs (red squares). For comparison, we report the data for passively evolving galaxies from Ilbert et al. (2010; cyan dotted line), Ilbert et al. (2013; purple dotted line), Brammer et al. (2011; black dotted line), and Moustakas et al. (2013; yellow filled star). We also report the lower limit estimate of the number density of compact ETGs by Valentinuzzi et al. (2010a; black upward arrow), fully compatible with our $z \sim 0$ estimate based on SDSS. Bottom panel: fraction of passive galaxies that are also compact (green triangles) and ultra-compact (red squares), as a function of the age of the universe or the redshift.

(A color version of this figure is available in the online journal.)

In Figure 5 we report the evolution of the number density of ETGs between $z = 3$ and $z = 1.2$ from this work, together with the same values at $0 < z < 1.2$ taken from C11. The only difference with C11 is that here we rebinned the data at $0 < z < 1.2$ in a slightly different manner, to better sample the range $0.1 < z < 0.7$, which covers about half of the age of the universe and was sampled with only one bin in C11. We stress that the uniqueness of this work is that we exploit for the first time a sample of ETGs complete down to $M_* = 10^{10} M_{\odot}$, extending the analysis of C11 up to $z \sim 3$, when the universe was just 2 Gyr old. We find that the number density of ETGs increases by a factor of 50 in a time span of only 3.5 Gyr, between $z \sim 3$ and $z \sim 1$. Thus, the epoch $1 < z < 3$ is critical for the buildup of the number of massive ETGs, in good agreement with, e.g., Ilbert et al. (2010, 2013) and with the phenomenological model of Peng et al. (2010). The number density of ETGs then further doubles in the 10 Gyr time span between $z \sim 1$ and $z \sim 0$, similarly to Ilbert et al. (2010), Franceschini et al. (2006), Cimatti et al. (2006), and Peng et al. (2010). Our measurements for the number density evolution of the global population of ETGs is in good agreement with Ilbert et al. (2010, 2013) and Brammer et al. (2011), obtained with much larger and less cosmic-variance-prone samples.

We see that the first ETGs to appear at $z \sim 3$ are virtually all compact or ultra-compact. The very rapid increase in the number density of the global population of ETGs between $z \sim 3$ and $z \sim 1$ is caused by the fast and steady increase of the number densities of all normal, compact, and ultra-compact ETGs. By $z \sim 1.5$, the normal ETGs become more numerous than the ultra-compact ones, and at $z \sim 1$ they are the most common ETGs, exceeding the number of compact ETGs.

After $z \sim 1$, the number density of normal ETGs keeps steadily increasing, albeit at a modest rate. At the same time, the evolution of compact and ultra-compact ETGs decouples from that of the large ETGs, with their number density steadily decreasing. In the local universe, the compact galaxies are (by definition, as they are defined to be 1σ below the local relation) 17% of the global population of ETGs, and the ultra-compact ones formally disappear almost completely by $z \sim 0$. However, it has been argued that the SDSS database may be biased against very compact galaxies (Scranton et al. 2002; Shih & Stockton 2011; Valentinuzzi et al. 2010a; Carollo et al. 2013). We note that our estimate of the number density of compact ETGs at $z \sim 0$ is ~ 5 times higher than the lower limit determined by Valentinuzzi et al. (2010a), thus formally in agreement, and that our new point at $z \sim 0.4$ seems to confirm the mild decrease. From $z \sim 1$ to $z \sim 0$ the number density of compact ETGs decreases by a factor of around two. The picture is less clear for the ultra-compact ETGs: the SDSS imaging does not offer enough spatial resolution to identify ultra-compact ETGs, and thus we indicate the number density of ultra-compact ETGs as a lower limit in Figure 5. The new point at $z \sim 0.4$ seems to support the fast decrease of the number density of ultra-compact ETGs at $0 < z < 1$, but the large error bar does not help to unambiguously fix the issue. In the end, the evolution seems to be strongly size-dependent, with a faster decrease for smaller ETGs, even though we cannot draw any strong conclusion due to the $z \sim 0$ uncertainties. This differential evolution is in quite good agreement with recent results by Carollo et al. (2013), who found a even milder decrease of the number density of ETGs with sizes smaller than 2 kpc (this is slightly larger than our “compactness” definition: according to our definition, ETGs of $M_* = 10^{10.5} M_\odot$ are compact if their size is smaller than 1 kpc).

6. DISCUSSION AND CONCLUSIONS

In this paper, we analyzed a sample of passive (SSFR $< 10^{-2} \text{ Gyr}^{-1}$) and massive ($M_* > 10^{10} M_\odot$) ETGs at $1.2 < z < 3$. The deep *H*-band imaging ensures that the sample is complete down to $M_* = 10^{10} M_\odot$, about an order of magnitude below M^* (Ilbert et al. 2010) and allows us to study the morphology of our galaxies in the optical rest frame up to $z \sim 3$. Moreover, the dense multiwavelength coverage ensures robust redshift measurements (for the objects without a spectroscopic redshift), accurate mass, and star formation activity determinations. The *Herschel* and *Spitzer* ancillary data allowed us to reinforce the passivity selection based on the SED fitting procedure.

The key findings of this paper are: (1) the identification up to $z \sim 3$ of passive and massive ETGs that dominate the red sequence (well defined up to $z \sim 2$, less clear at $2 < z < 3$; see Figure 2); (2) the accurate determination, with the evolution of the average size of ETGs at $0 < z < 3$, reported in Figure 4; and (3) the robust determination of the differential evolution of the spatial abundance of massive, i.e., stellar mass $M_* > 10^{10} M_\odot$, passive galaxies as a function of redshift and as a function of

the their size, a proxy of their average projected central stellar density, shown in Figure 5.

At high redshift, i.e., $z \sim 3$, the size distribution of ETGs is heavily tilted toward small sizes, and massive and passive galaxies are predominantly high-stellar-density systems. This implies that the mechanism through which these galaxies accrete their mass and eventually become passive at those early epochs leaves a remnant that is very compact (Cimatti et al. 2008). Many different mechanisms leading to the formation of compact remnants have been proposed in literature: Dekel et al. (2009b) argued that disk instabilities lead to the formation of compact remnants; Hopkins et al. (2008), Wuyts et al. (2010), and Bournaud et al. (2011) showed that gas-rich mergers can form compact galaxies; Johansson et al. (2012) proposed that compact galaxies can be formed by in situ star formation driven by cold flows.

By $z \sim 1$ the abundance of small ETGs reaches its peak, followed by a decline, apparently faster for the ultra-compact than for the compact ones (see Section 5 and discussion of the uncertainties for $z < 0.5$). Apparently, whatever set of mechanisms was producing ultra-compact passive galaxies at $1 \lesssim z \lesssim 2.5$ is no longer working at later epochs. Moreover, the size distribution of the new ETGs that become passive between $z \sim 1$ and $z \sim 0$ is gradually moving toward larger sizes, implying that the mechanism through which star formation is quenched in these massive ETGs acts in such a way as to leave larger quenched remnants as (cosmic) time goes by, a tendency which accelerates at $z < 1$. This may be a natural consequence of the inside-out growth of the disks (a widely entertained notion, Samland & Gerhard 2003; Brook et al. 2006; Muñoz-Mateos et al. 2011), with such disks being the likely precursors to passive ETGs. So, bigger disks would leave bigger ETG remnants.

In the $0 < z < 1$ epoch the average size of the ETGs steadily increases (see Figure 4). This evolution might be due to two different mechanisms (or a mix of the two): on one hand, the individual ETGs increase in size, by minor merging or accretion; on the other hand new already large ETGs, which never passed through the compact or ultra-compact phase, appear. In this respect, the evolution of the number densities of ETGs of different sizes, constrained in Figure 5, can help to weigh the relative importance of two mechanisms. In particular, even assuming that all the disappearing compact and ultra-compact ETGs are transformed in ETGs of normal size and density, in a cascade of merging and interactions to form normal-sized galaxies (e.g., Huang et al. 2013), Figure 5 shows that they are not numerous enough to support the increase of the total number of normal ETGs observed over the same time interval. In fact, between $z \sim 1$ and $z \sim 0$ the number density all ETGs increases by about $\sim 0.8 \times 10^{-3} \text{ Mpc}^{-3}$, while the number density of compact ETGs that disappear is only $\sim 0.3 \times 10^{-3} \text{ Mpc}^{-3}$. This implies that the observed rate at which compact galaxies disappear cannot sustain the observed increase of the number of normal ETGs; thus the growth of the individual ETGs is not the dominant mechanism causing the average size of ETGs to increase (Figure 4), in agreement with Carollo et al. (2013).

At the same time, the decrease of the number density of compact and ultra-compact ETGs between $z \sim 1$ and $z \sim 0$ indicates that a fraction of these galaxies either become active, because of a sudden refurbishment of fresh gas, or—more likely—they grow in size, via minor merging or smooth accretion, becoming normal-sized ETGs. Hopkins et al. (2009) and Petty et al.

(2013) come to the conclusion that the properties of local ETGs are indeed compatible with an inside-out growth.

Before concluding, we also wish to comment on the cosmic rise and fall of the ultra-compact passive galaxies that this paper has documented. The extreme compactness and large stellar mass of these galaxies argue against hierarchical merging of stellar systems as the primary mechanism for the assembly of their stellar mass (M. Giavalisco et al., in preparation). Rather, it is likely that they emerged in their final state after the quenching of star-forming galaxies of the same size and density. In this case the rise and fall of ultra-compact ETGs are the result of four different processes: (1) the rate at which ultra-compact star-forming galaxies form in this mass range (roughly $M_* > 10^{10} M_\odot$); (2) the rate at which they are destroyed before they are quenched, i.e., they are transformed from ultra-compact galaxies into galaxies of lower density by merging and interactions; (3) the rate at which the ultra-compact star-forming galaxies shut down star formation and become passive; and (4) the rate at which the ultra-compact passive galaxies are transformed into galaxies of lower stellar density by merging and interactions. Mechanisms (1) and (2), although not directly constrained by this work, define the “reservoir” of compact star-forming galaxies from which compact ETGs can form; the effects of mechanisms (3) and (4) in shaping the number density evolution of compact ETGs have been extensively discussed in this paper.

Interestingly, Wuyts et al. (2011) and Barro et al. (2013) identified a rich population of compact star-forming galaxies at $1.5 < z < 3$, whose number densities and physical properties are compatible with being the progenitors of the compact and ultra-compact ETGs. The authors speculate that those compact star-forming galaxies are formed from a gas-rich process (merger or disk instabilities) that at first induces a compact starburst and then feeds an AGN, which quenches star formation, turning these objects into compact ETGs. They find that these compact star-forming objects are very rare at $z < 1.5$, supporting our conjecture that after that epoch the mechanism through which ETGs are formed produces a large remnant. However, the definition of ETGs in Barro et al. (2013), as well as the definition of which star-forming galaxies can transform into ETGs, differ from ours. So, we looked for progenitors of our ETGs in a companion paper, Williams et al. (2013): we have identified a sample of compact star-forming galaxies which may be progenitors of our high-redshift passive sample (which represents some of the first ETGs to appear in the universe). This sample has consistent SFRs and stellar masses with our ETGs, and are evolutionarily consistent assuming physically motivated SFHs. This sample demonstrates that massive and active enough compact SF galaxies exist at $z > 3$ to account for the number density of compact ETGs presented here, assuming mass buildup by purely in situ star formation, further justifying the evolutionary link between compact SF and compact passive galaxies.

To summarize, our main findings are as follows.

1. We find that at $1 < z < 3$, the passively evolving ETGs are the reddest and most massive objects in the universe. This implies that an embryo of the Hubble sequence, in the sense of a correlation between morphology, mass, color, and star formation activity of galaxies, is already in place at $z \sim 3$. We observe a scarcity of ETGs with $M_* < 10^{10.5} M_\odot$, with the majority of our ETGs having $M_* > 10^{10.5} M_\odot$. Since we accurately set our mass completeness to $M_* = 10^{10} M_\odot$, we can conclude that that scarcity is not due to

an observational bias. Hence, at $z > 1.2$ the mechanism producing ETGs leaves a remnant that is preferentially very massive. This result reinforces previous claims for a “downsizing” pattern of the mass assembly of ETGs. A possible interpretation is that at that early epoch the process that suddenly quenches the star formation activity in some objects, transforming them into passively evolving ETGs, is preferentially effective for objects with stellar mass above $M_* = 10^{10.5} M_\odot$. This result is in qualitative agreement with Peng et al. (2010), who highlighted the prominent role of mass quenching at high redshift.

2. We measure a significant evolution of the mass–size relation of ETGs from $z \sim 3$ to $z \sim 1$, with the average size of galaxies increasing by roughly a factor of ~ 2 over this redshift interval, corresponding to 3 Gyr of cosmic time. The evolution of the size of ETGs is faster for galaxies with $M_* > 10^{10.5} M_\odot$ than for those with $M_* < 10^{10.5} M_\odot$. About 90% (70%) of the ETGs at $z > 2$ are compact (ultra-compact). We find that the average size of ETGs between $z \sim 3$ and $z \sim 0$ evolves with the redshift following a simple power law $r_e \sim (1+z)^\alpha$, with $\alpha = -1.18 \pm 0.15$. If ETGs with $M \leq 10^{10.5} M_\odot$ are fitted separately, we find a marginally steeper power α for the most massive ETGs ($\alpha = -1.33 \pm 0.18$), indicating a faster size evolution.
3. We witness the buildup of the most massive ETGs, with their number density increasing by 50 times between $z \sim 3$ and $z \sim 1$. We find that 90% of ETGs at $z > 2$ are compact or ultra-compact, indicating that the event through which such first ETGs accrete their mass leaves a remnant that is very compact. As the cosmic time goes by, new ETGs tend to be increasingly larger, with the “normal”-sized ETGs (meaning those objects with sizes comparable to the local ETGs of the same mass) becoming the most common ETGs at $z \sim 1$. At $z > 1$ the mechanisms creating new ultra-compact ETGs prevail on those destroying them (merging, smooth accretion), resulting in a net increase of their number density; at $z < 1$ the balance between such mechanisms inverts, with the processes decreasing the stellar density of ultra-compact galaxies finally prevailing. Thus, the number density of compact passive ETGs starts decreasing, although the measure of such decrease to $z = 0$ remains quite uncertain. Still, such a decrease would not account for the increased number of “normal”-size galaxies, even if all the compact, passive ETGs at $z = 1$ were to disappear by $z = 0$. Therefore, the evolution of the average size of ETGs at $0 < z < 1$ is mainly due to the appearance of newly quenched ETGs that are born large, rather than to the size increase of individual galaxies.

P.C. acknowledges support from ERC advanced grant ERC-2010-AdG-268107-EARLY.

REFERENCES

- Arnouts, S., Walcher, C. J., Le Fèvre, O., et al. 2007, *A&A*, 476, 137
 Baldry, I. K., Glazebrook, K., Brinkmann, J., et al. 2004, *ApJ*, 600, 681
 Barro, G., Faber, S. M., Perez-Gonzalez, P. G., et al. 2013, *ApJ*, 765, 104
 Bell, E. F., van der Wel, A., Papovich, C., et al. 2012, *ApJ*, 753, 167
 Bell, E. F., Wolf, C., Meisenheimer, K., et al. 2004, *ApJ*, 608, 752
 Blanton, M. R., Schlegel, D. J., Strauss, M. A., et al. 2005, *AJ*, 129, 2562
 Bournaud, F., Chapon, D., Teyssier, R., et al. 2011, *ApJ*, 730, 4
 Brammer, G. B., Whitaker, K. E., van Dokkum, P. G., et al. 2011, *ApJ*, 739, 24
 Brook, C. B., Kawata, D., Martel, H., et al. 2006, *ApJ*, 639, 126
 Bruzual, G., & Charlot, S. 2003, *MNRAS*, 344, 1000
 Buitrago, F., Trujillo, I., Conselice, C. J., et al. 2008, *ApJL*, 687, L61

- Bundy, K., Ellis, R. S., Conselice, C. J., et al. 2006, *ApJ*, 651, 120
- Calzetti, D., Armus, L., Bohlin, R. C., et al. 2000, *ApJ*, 533, 682
- Carollo, C. M., Bschorr, T. J., Renzini, A., et al. 2013, *ApJ*, 773, 112
- Cassata, P., Cimatti, A., Kurk, J., et al. 2008, *A&A*, 483, L39
- Cassata, P., Giavalisco, M., Guo, Y., et al. 2011, *ApJ*, 743, 96
- Cimatti, A., Cassata, P., Pozzetti, L., et al. 2008, *A&A*, 482, 21
- Cimatti, A., Daddi, E., & Renzini, A. 2006, *A&A*, 453, 29
- Cimatti, A., Nipoti, C., & Cassata, P. 2012, *MNRAS*, 422, 62
- Daddi, E., Renzini, A., Pirzkal, N., et al. 2005, *ApJ*, 626, 680
- Dahlen, T., Mobasher, B., Faber, S., et al. 2013, *ApJ*, submitted
- Damjanov, I., Abraham, R. G., Glazebrook, K., et al. 2011, *ApJ*, 739, 44
- Dekel, A., Birnboim, Y., Engel, G., et al. 2009a, *Natur*, 457, 451
- Dekel, A., Sari, R., & Ceverino, D. 2009b, *ApJ*, 703, 785
- Elbaz, D., Dickinson, M., Hwang, H. S., et al. 2011, *A&A*, 533, 119
- Faber, S. M., Willmer, C. N. A., Wolf, C., et al. 2007, *ApJ*, 665, 265
- Fioc, M., & Rocca-Volmerange, B. 1997, *A&A*, 326, 950
- Förster-Schreiber, N. M., Genzel, R., Bouché, N., et al. 2009, *ApJ*, 706, 1364
- Franceschini, A., Rodighiero, G., Cassata, P., et al. 2006, *A&A*, 453, 397
- Genzel, R., Burkert, A., Bouché, N., et al. 2008, *ApJ*, 687, 59
- Giavalisco, M., Dickinson, M., Ferguson, H. C., et al. 2004, *ApJ*, 600, 103
- Gobat, R., Strazzullo, V., Daddi, E., et al. 2012, *ApJ*, 759, 44
- Grogin, N. A., Kocevski, D. D., Faber, S. M., et al. 2011, *ApJS*, 197, 35
- Guo, Y., Ferguson, H. C., Giavalisco, M., et al. 2013, *ApJS*, 207, 24
- Guo, Y., Giavalisco, M., Cassata, P., et al. 2012, *ApJ*, 749, 149
- Hopkins, P. F., Bundy, K., Murray, N., et al. 2009, *MNRAS*, 398, 898
- Hopkins, P. F., Hernquist, L., Cox, T., et al. 2008, *ApJ*, 688, 757
- Huang, S., Ho, L. C., Peng, C. Y., et al. 2013, *ApJ*, 766, 47
- Ilbert, O., McCracken, H. J., Le Fèvre, O., et al. 2013, *A&A*, 556, 55
- Ilbert, O., Salvato, M., Le Flocc'h, E., et al. 2010, *ApJ*, 709, 644
- Johansson, P. H., Naab, T., & Ostriker, J. P. 2012, *ApJ*, 754, 115
- Khochfar, S., & Silk, J. 2006, *ApJL*, 648, L21
- Koekemoer, A. M., Faber, S. M., Ferguson, H. C., et al. 2011, *ApJS*, 197, 36
- Kurk, J., Cimatti, A., Daddi, E., et al. 2013, *A&A*, 549, 63
- Laidler, V. G., Papovich, C., Grogin, N. A., et al. 2007, *PASP*, 119, 1325
- López-Sanjuan, C., Le Fèvre, O., & Ilbert, O. 2012, *A&A*, 548, 7
- Maraston, C., Pforr, J., Renzini, A., et al. 2010, *MNRAS*, 407, 830
- Marchesini, D., Van Dokkum, P. G., Förster-Schreiber, N. M., et al. 2009, *ApJ*, 701, 1765
- Moustakas, J., Coil, A. L., Aird, J., et al. 2013, *ApJ*, 767, 50
- Muñoz-Mateos, J. C., Boissier, S., Gil de Paz, A., et al. 2011, *ApJ*, 731, 10
- Naab, T., Johansson, P. H., & Ostriker, J. P. 2009, *ApJ*, 699, 178
- Naab, T., Johansson, P. H., Ostriker, J. P., et al. 2007, *ApJ*, 658, 710
- Newman, A. B., Ellis, R. S., Bundy, K., & Treu, T. 2012, *ApJ*, 746, 162
- Nipoti, C., Treu, T., Leauthaud, A., et al. 2012, *MNRAS*, 422, 1714
- Nonino, M., Dickinson, M., Rosati, P., et al. 2009, *ApJS*, 183, 244
- Oser, L., Naab, T., Ostriker, J. P., et al. 2012, *ApJ*, 744, 63
- Peng, C. Y., Ho, L. C., Impey, C. D., et al. 2002, *AJ*, 124, 266
- Peng, Y., Lilly, S. J., Kovac, K., et al. 2010, *ApJ*, 721, 193
- Peng, Y., Lilly, S. J., Renzini, A., & Carollo, M. 2012, *ApJ*, 757, 4
- Petty, S. M., Neill, J. D., Jarrett, T. H., et al. 2013, *AJ*, 146, 77
- Poggianti, B. M., Calvi, R., Bindoni, D., et al. 2012, *ApJ*, 762, 77
- Popesso, P., Dickinson, M., Nonino, M., et al. 2009, *A&A*, 494, 443
- Pozzetti, L., Bolzonella, M., Zucca, E., et al. 2010, *A&A*, 523, 13
- Ravindranath, S., Giavalisco, M., Ferguson, H. C., et al. 2006, *ApJ*, 652, 963
- Renzini, A. 2006, *ARA&A*, 44, 141
- Ryan, R. E., Jr., McCarthy, P. J., Cohen, S. H., et al. 2012, *ApJ*, 749, 53
- Salimbeni, S., Fontana, A., Giallongo, E., et al. 2009, in *AIP Conf. Proc.* 1111, Probing Stellar Populations Out to the Distant Universe, ed. G. Giobbi et al. (Melville, NY: AIP), 207
- Salpeter, E. E. 1955, *ApJ*, 121, 161
- Samland, M., & Gerhard, O. E. 2003, *A&A*, 399, 961
- Scranton, R., Johnston, D., Dodelson, S., et al. 2002, *ApJ*, 579, 48
- Shankar, F., Marulli, F., Bernardi, M., et al. 2010, *MNRAS*, 405, 948
- Shankar, F., Marulli, F., Bernardi, M., et al. 2013, *MNRAS*, 428, 109
- Shih, H., & Stockton, A. 2011, *ApJ*, 733, 45
- Toft, S., van Dokkum, P., Franx, M., et al. 2007, *ApJ*, 671, 285
- Trujillo, I., Conselice, C. J., Bundy, K., et al. 2007, *MNRAS*, 382, 109
- Valentinuzzi, T., Fritz, J., Poggianti, B., et al. 2010a, *ApJ*, 712, 226
- Valentinuzzi, T., Poggianti, B. M., Saglia, R. P., et al. 2010b, *ApJL*, 721, L19
- van der Wel, A., Bell, E. F., Häussler, B., et al. 2012, *ApJS*, 203, 24
- van der Wel, A., Rix, H.-W., Wuyts, S., et al. 2011, *ApJ*, 730, 38
- Van Dokkum, P. G., Franx, M., Kriek, M., et al. 2008, *ApJL*, 677, L5
- Vanzella, E., Cristiani, S., Dickinson, M., et al. 2008, *A&A*, 478, 83
- Weinzirl, T., Jogee, S., Conselice, C. J., et al. 2011, *ApJ*, 743, 87
- Whitaker, K. E., Labbé, I., van Dokkum, P. G., et al. 2011, *ApJ*, 735, 86
- Williams, C. C., Giavalisco, M., Cassata, P., et al. 2013, *ApJ*, submitted
- Windhorst, R. A., Cohen, S. H., Hathi, N. P., et al. 2011, *ApJS*, 193, 27
- Wuyts, S., Cox, T., Hayward, C. C., et al. 2010, *ApJ*, 722, 1666
- Wuyts, S., Förster Schreiber, N. M., van der Wel, A., et al. 2011, *ApJ*, 742, 96
- Zirm, A. W., van der Wel, A., Franx, M., et al. 2007, *ApJ*, 656, 66